Journal of Biomolecular NMR, **24:** 301–316, 2002.
KLUWER/ESCOM

Backbone dynamics of the cytotoxic Ribonuclease α-sarcin by ^{15}N NMR relaxation methods

José Manuel Pérez-Cañadillas[a,*], Marc Guenneugues[b,**], Ramón Campos-Olivas[a,***], Jorge Santoro[a], Alvaro Martínez del Pozo[c], José G. Gavilanes[c], Manuel Rico[a] & Marta Bruix[a,****]
[a]*Instituto de Química Física 'Rocasolano', Consejo Superior de Investigaciones Científicas, Serrano 119, 28006 Madrid, Spain;* [b]*Bijvoet Center for Biomolecular Research, Utrecht University, Padualaan 8, 3584 CH Utrecht, The Netherlands;* [c]*Departamento de Bioquímica y Biología Molecular I, Facultad de Química, Universidad Complutense, 28040 Madrid, Spain*

Received 7 June 2002; Accepted 26 September 2002

Key words: α-sarcin, model-free analysis, NMR relaxation, protein dynamics, reduced spectral density mapping

Abstract

The cytotoxic ribonuclease α-sarcin is a 150-residue protein that inactivates ribosomes by selectively cleaving a single phosphodiester bond in a strictly conserved rRNA loop. In order to gain insights on the molecular basis of its highly specific activity, we have previously determined its solution structure and studied its electrostatics properties. Here, we complement those studies by analysing the backbone dynamics of α-sarcin through measurement of longitudinal relaxation rates R_1, off resonance rotating frame relaxation rates $R_1\rho$, and the $^{15}N\{^1H\}$ NOE of the backbone amide ^{15}N nuclei at two different magnetic field strengths (11.7 and 17.6 T). The two sets of relaxation parameters have been analysed in terms of the reduced spectral density mapping formalism, as well as by the model-free approach. α-Sarcin behaves as an axial symmetric rotor of the prolate type ($D_\parallel/D_\perp = 1.16 \pm 0.02$) which tumbles with a correlation time τ_m of 7.54 ± 0.02 ns. The rotational diffusion properties have been also independently evaluated by hydrodynamic calculations and are in good agreement with the experimental results. The analysis of the internal dynamics reveals that α-sarcin is composed of a rigid hydrophobic core and some exposed segments which undergo fast (ps to ns) internal motions. Slower motions in the μs to ms time scale are less abundant and in some cases can be assigned to specific motional processes. All dynamic data are discussed in relation to the role of some particular residues of α-sarcin in the process of recognition of its ribosomal target.

Introduction

Since α-sarcin was first discovered (Olson and Goerner, 1965), it has been heralded as a promising antitumoral agent (Turnay et al., 1993; Olmo et al., 2001) and as a tool to study ribosome structure and function (Wool, 1984). α-Sarcin's cytotoxicity relies on its striking ability to recognise and selectively cleave a single phosphodiester bond within the 23S ribosomal RNA, in a strictly conserved region which is also targeted by ricin related proteins, and therefore named as α-sarcin/ricin domain (SRD). The SRD is the Achilles heel of the ribosome, as it is also the binding site of various elongation factors and the disruption of its 3D structure by α-sarcin leads to astonishing loss of functionality and eventually to cell death. The protein also has the ability to translocate across cytoplasm membranes which have been altered or damaged by processes such as viral infection, malignant transformation or addition of toxic agents (Wool, 1997).

*Present addresses: Medical Research Council, Laboratory of Molecular Biology, Hills Road CB2 2QH, Cambridge, U.K.
**ENTOMED S.A., rue Tobias Stimner, 67400, Illkirch, France.
***Structural and Computational Biology Program. Centro Nacional de Investigaciones Oncológicas, Melchor Fernández Almagro 3, 28029 Madrid, Spain.
****To whom correspondence should be addressed. E-mail: mbruix@iqfr.csic.es

We have recently described the 3D structure of α-sarcin (Pérez-Cañadillas et al., 2000) and its electrostatic properties (Pérez-Cañadillas et al., 1998). These studies unravelled some key issues such as the catalytic mechanism which has since been corroborated by biochemical data (Lacadena et al., 1999), and allowed us to propose a binding mode to the SRD. The dynamic properties of both substrate and receptor play a central role in any complex formation. Theories like induced fit call for a certain degree of flexibility in the substrate, the receptor, or both. Flexibility is often associated with interfaces, and it is well established that the complex formation can lead to dramatic dynamic and conformational changes (Mittermaier et al., 1999; Wang et al., 2001). Protein residues involved in molecular recognition tend to be dynamic hot spots (Clackson et al., 1995; Atwell et al., 1997; Feher and Cavanagh 1999). Regions with motions of a wide range of amplitudes and time scales form the landscape of molecular interfaces. Internal motions allow recognition elements to screen a significant part of the conformational space at minimum energy cost, increasing the chances of a successful binding. NMR is a suitable technique to study dynamics because it can not only report on movements occurring over a wide time scale (from pico-seconds to hours), but it also provides information at a specific atomic site. ^{15}N relaxation of the amide protons provides information in the pico-second to mili-second range, which is potentially relevant for recognition processes (for a recent review see Korzhnev et al., 2001). Here we describe the protein backbone dynamics of α-sarcin, analysed in terms of the reduced spectral density mapping, as well as the model-free approach, and hydrodynamic calculations. In combination with our previous studies on the structure (Pérez-Cañadillas et al., 2000) and electrostatic properties (Pérez-Cañadillas et al., 1998), the results presented here represent a significant improvement in understanding the factors that determine the specificity and the mode of action of α-sarcin at the molecular level.

Materials and methods

NMR samples

Uniform [U-^{15}N] recombinant α-sarcin was obtained and purified as described elsewhere (Lacadena et al., 1994) by growing *E. coli* RB791 cells in M9 minimal media, using $^{15}NH_4Cl$ as primary source of nitrogen. All the NMR experiments described here were recorded from a single NMR sample at pH 6.0 and 308 K temperature. The sample was prepared by dissolving [U-^{15}N] labelled protein in a mixture 90% H_2O/10% ^2H_2O to a final protein concentration around 1.5 mM.

NMR spectroscopy

The NMR experiments were acquired at the SON Large Scale Facility of Utrecht University in a Varian Unity plus 750 MHz and a Varian Unity 500 MHz spectrometers with external magnetic field intensities of 17.6 and 11.7 T, respectively, both equipped with triple resonance probes and pulsed field gradients units.

The ^{15}N longitudinal relaxation rates (R_1) were obtained from series of standard inversion-recovery experiments (Farrow et al., 1994). The 17.6 T data set is composed of 10 different experiments, with relaxation delays ranging from 0 to 1500 ms, while the 11.7 T set is formed by 12 experiments, with relaxation delays from 0 to 1200 ms. Both series of experiments were acquired in two single interleaved matrices to ensure uniformity of the experimental conditions.

The ^{15}N transverse relaxation was studied on the basis of off-resonance $R_{1\rho}$ values. At 17.6 T we have used on-resonance hard spin-lock RF pulses (Szyperski et al., 1993) with a field strength of 1420 Hz, placed in the centre of the ^{15}N amide region (118.79 ppm). Twelve intensity modulated experiments were recorded with relaxation delays between 0 and 250 ms. A different approach was followed for the 11.7 T data, using off-resonance amplitude and frequency modulated adiabatic pulses (Akke and Palmer, 1996; Zinn-Justin et al., 1997; Banci et al., 1998; Mulder et al., 1998), and repeating the measurements at different ^{15}N offsets. In both cases B_1 field strength and offset (Δ) determine the effective field (ω_{eff}) experienced by a particular spin according to the equation: $\omega_{eff} = 2\pi(B_1^2 + \Delta^2)^{1/2}$. Seven independent off-resonance $R_{1\rho}$ values (at 11.7 T) were determined by using a B_1 spin-lock field of 1490 Hz strength at offsets ($\Delta = -3000, -2000, -1000$, 0, 1000, 2500 and 3500 Hz) from the centre of the ^{15}N spectrum. These offset values correspond to 26.4, 36.7, 56.1, 90.0, 56.1, 30.8 and 23.06 nominal tilt angles ($\theta = \tan^{-1}(\omega_1/\Delta)$) relative to the direction of the static magnetic field. Each set of off-resonance $R_{1\rho}$ comprised 13 experiments, with relaxation delays ranging between 0 and 350 ms, recorded in interleaved

mode. A recycling delay of 2.0 s was used in these experiments.

Heteronuclear $^{15}N\{^1H\}$ NOE were determined from the ratio of two experiments with and without saturation as described previously (Farrow et al., 1995, Mulder et al., 1999). Longer recycling delays were used for these experiments (10 s and 5 s for the 17.6 and 11.7 T data sets) to avoid saturation transfer.

The heteronuclear experiments described above were collected with 512 × 512 points. The ^{15}N spectral widths were 3003 and 2000 Hz, and 5400 and 4000 Hz for the ^1H dimension (for 17.6 and 11.7 T data sets, respectively). All the experiments (129) were processed with the nmrPipe software (Delaglio et al., 1995) and analysed with ANSIG (Kraulis, 1989; Kraulis et al., 1994).

Reduced spectral density mapping

Two main mechanisms account for ^{15}N amide relaxation: dipolar coupling with its covalently bound proton and ^{15}N chemical shift anisotropy (Abragam, 1961). The spectral density function of each individual ^1H-^{15}N amide vector is closely related to its dynamic behaviour. The relaxation rates in a two-spin system can be expressed as linear combinations of J(ω) (spectral density function) values at five frequencies namely: 0, ω_N, $\omega_H-\omega_N$, ω_H and $\omega_H+\omega_N$ (see for example Peng and Wagner, 1992a,b). With the approximation of replacing the high frequency terms by a single average term ($0.87\omega_H$) (Farrow et al., 1995), it is possible to map the spectral density function using only the classical relaxation data: R_1, $R_{1\rho}$ (90°) (or R_2) and $^{15}N\{^1H\}$-NOE. The following matrix show this relationship.

$$\begin{bmatrix} J(0) \\ J(\omega_N) \\ J(0.87\omega_H) \end{bmatrix} = \begin{bmatrix} \frac{-3}{4(2d^2+c^2)} & \frac{3}{2(3d^2+c^2)} & \frac{-9}{10(3d^2+c^2)} \\ \frac{1}{(3d^2+c^2)} & 0 & \frac{-7}{5(3d^2+c^2)} \\ 0 & 0 & \frac{1}{5d^2} \end{bmatrix} \otimes \begin{bmatrix} R_1 \\ R_{1\rho}\,(90°) \\ R_N\,(H_Z \rightarrow N_Z) \end{bmatrix} \quad (1)$$

$$d^2 = \left(\frac{\mu_0 \hbar \gamma_N \gamma_H}{8\pi r_{NH}^3}\right)^2,\ c^2 = \tfrac{1}{3}(\omega_N \Delta\sigma)^2$$

$$R_N\,(H_Z \rightarrow N_Z) = \gamma_N/\gamma_H \cdot R_1 \cdot [NOE - 1].$$

A FORTRAN program was used to calculate two different sets of J(0), J(ω_N) and J($0.87\omega_H$) values, corresponding to the two different field values; errors were estimated by Monte Carlo methods. In total, five spectral frequencies were mapped (0, 50, 75, 434 and 653 MHz). The J(0) values are affected by adiabatic processes in the μs to ms time scale particularly chemical exchange processes. The exchange factors Φ were extracted from the two independently determined J(0) sets using the following equation (Peng and Wagner, 1995):

$$\Phi = \frac{J_{obs1}(0) - J_{obs2}(0)}{\lambda_1 \omega_{N1}^2 - \lambda_2 \omega_{N2}^2}. \quad (2)$$

The overall correlation time of α-sarcin was obtained from one of the roots of the Lefèvre equation (Lefèvre et al., 1996).

$$2\alpha\omega_N^2\tau^3 + 5\beta\omega_N^2\tau^2 + 2(\alpha - 1)\tau + 5\beta = 0 \quad (3)$$

The parameters α and β were obtained from the linear fitting of J(ω_N) versus J(0) for the two independent data sets (11.7 and 17.6 T).

Model-free analysis

The relaxation data were also analysed in terms of the model-free approach (Lipari and Szabo, 1982), extended to account for fast internal motions occurring in two distinctive time scales (Clore et al., 1990) and rotational diffusion anisotropy (Woessner, 1962). The spectral density functions were finally modelled according to the following general equation:

$$J(\omega) = \tfrac{2}{5}\sum_i A_i \left[\frac{S_f^2 S_s^2 \tau_i}{1 + (\omega\tau_i)^2} + \frac{(1 - S_f^2)\,\tau_{f,i}}{1 + (\omega\tau_{f,i})^2} + \frac{S_f^2 (1 - S_s^2)\,\tau_{s,i}}{1 + (\omega\tau_{s,i})^2} \right], \quad (4)$$

$$\begin{aligned} A_1 &= \tfrac{1}{4}\left(3\cos^2(\theta) - 1\right)^2 & \tau_1 &= 6D_\perp, \\ A_2 &= \tfrac{3}{4}\sin^2(2\theta) & \tau_2 &= 5D_\perp + D_{||}, \\ A_3 &= \tfrac{3}{4}\sin^4(\theta) & \tau_3 &= 2D_\perp + 4D_{||}, \end{aligned}$$

$$S^2 = S_f^2 S_s^2;\ \tau_{f,i}^{-1} = \tau_m^{-1} + \tau_f^{-1};\ \tau_{s,i}^{-1} = \tau_m^{-1} + \tau_s^{-1}.$$

Order parameters S_s^2 and S_f^2 appear in situations with distinctive fast and very fast internal motions with effective correlation times given by τ_s and τ_f. Rotational anisotropy is introduced in the model by the coefficients A_i and correlation times τ_1, τ_2 and τ_3 (the equations represent the case in which the tumbling is axially symmetric).

We have used the program Modelfree 4.01 (Mandel et al., 1995; Palmer et al., 1991) to perform the model-free analysis. Firstly, isotropic and anisotropic rotational diffusion models were evaluated for a selected subset of spins (59) having heteronuclear NOEs over 95% of the theoretical maximum and $R_{1\rho}(90°)$ values within one standard deviation of the mean. Five hundred Monte Carlo simulations were done for each diffusion model and the χ^2 values were compared by F-statistics to select the proper model as described (Lee et al., 1997). The internal dynamics were explored afterwards with five spectral density functions (1: S^2, 2: S^2, τ_e, 3: S^2, R_{ex}, 4: S^2, τ_e, R_{ex} and 5: S_f^2, S_s^2, τ_e). As in the diffusion model exploration, Monte Carlo simulations (500) and F-statistics were used for the internal dynamics model selection as described elsewhere (Mandel et al., 1995). Model 5 takes into account a situation with two distinctive internal motions (with at least 2 or 3 orders of magnitude between their time constants) both faster than τ_m. The order parameters S_f^2 and S_s^2 reflect the amplitude of the two internal motions, being τ_e the time constant for the slower one. Discarding the existence of the faster of the two 'fast' internal motions ($S_f^2 = 1$) simplifies the equation to, the one for model 2, and a further assumption ($\tau'_e \approx \tau_m$) leads to model 1 in which no internal motions faster than τ_m are accounted for. Finally models 3 and 4 correspond to 1 and 2 but with the $R_{1\rho}(90°)$ values corrected by an exchange term R_{ex}.

Off-resonance $R_{1\rho}$ relaxation

The dependence of the off-resonance $R_{1\rho}$ values with the tilt angles was fitted to the following equation:

$$R_{1\rho} = R_1 \cos^2\theta + (R_2 + R_{ex}) \sin^2\theta \quad (5)$$

where R_2 stands only for the CSA and dipolar contributions to the transverse relaxation rates. The exchange contribution to transverse relaxation, R_{ex} can be expressed in the case of the simplest two site model as:

$$R_{ex} = p_A p_B \Delta\omega^2 \frac{\tau_{ex}}{1 + (\tau_{ex}\omega_{eff})^2} \quad (6)$$

where p_A and p_B represent the relative populations of the two states with a chemical shift difference $\Delta\omega$. Assuming this two-site exchange model, the time constant (τ_{ex}) of the process can be obtained from the fitting of the corrected $R_{1\rho}$ against the effective frequency ω_{eff} of the spin-lock field:

$$\frac{\left(R_{1\rho}(\theta) - R_1 \cos^2\theta\right)}{\sin^2\theta} = R_{1\rho}\left(90°\right) = R_2 + p_A p_B \Delta\omega^2 \frac{\tau_{ex}}{1 + (\tau_{ex}\omega_{eff})^2}. \quad (7)$$

Hydrodynamic calculations.

A theoretical estimation of the diffusion parameters and NMR relaxation data has been performed by using the program HYDRONMR (García de la Torre et al., 2000) based on the bead-model method (for a recent review see Carrasco and García de la Torre, 1999). The program computes the full 6×6 diffusion tensor from which the translational and rotational components can be easily calculated and compared with the experimental values that can be obtained by NMR relaxation and diffusion studies. Additionally, the program (see above) also calculates relaxation parameters (T_1, T_2 and NOE) for each amino acid residue in the absence of internal dynamic processes. All the calculations were made using the first conformer in the α-sarcin PDB file (1DE3, Pérez-Cañadillas et al., 2000), at a temperature of 308 K and solvent viscosity of 0.72 cp (calculated with Equation 19 of García de la Torre et al., 2000). The atomic element radius (AER) was obtained following a recently proposed protocol (Bernadó et al., 2002) based on a comparison between experimental and calculated data for various AERs. As they have observed that the inclusion of residues in flexible regions can negatively influence the outcome of hydrodynamic calculations, the first two N-terminal residues of α-sarcin (which showed no structural preferences) have been excluded from the calculation.

Results

^{15}N NMR relaxation has been used to characterise α-sarcin internal backbone dynamics. Figure 1 shows the α-sarcin sequential distribution of the experimental parameters: longitudinal relaxation rate R_1, rotating frame transverse relaxation rate $R_{1\rho}(90°)$ and the heteronuclear $^{15}N\{^1H\}$ steady-state NOE, measured at two different magnetic fields of 17.6 and 11.7 T. Mean R_1, $R_{1\rho}(90°)$ and $^{15}N\{^1H\}$-NOE values are 2.0 s^{-1}, 9.7 s^{-1} and 0.74 at 11.7 T, and 1.2 s^{-1}, 12.4 s^{-1} and 0.79 at 17.6 T. The regular secondary elements of α-sarcin show, in general, high $^{15}N\{^1H\}$-NOE values,

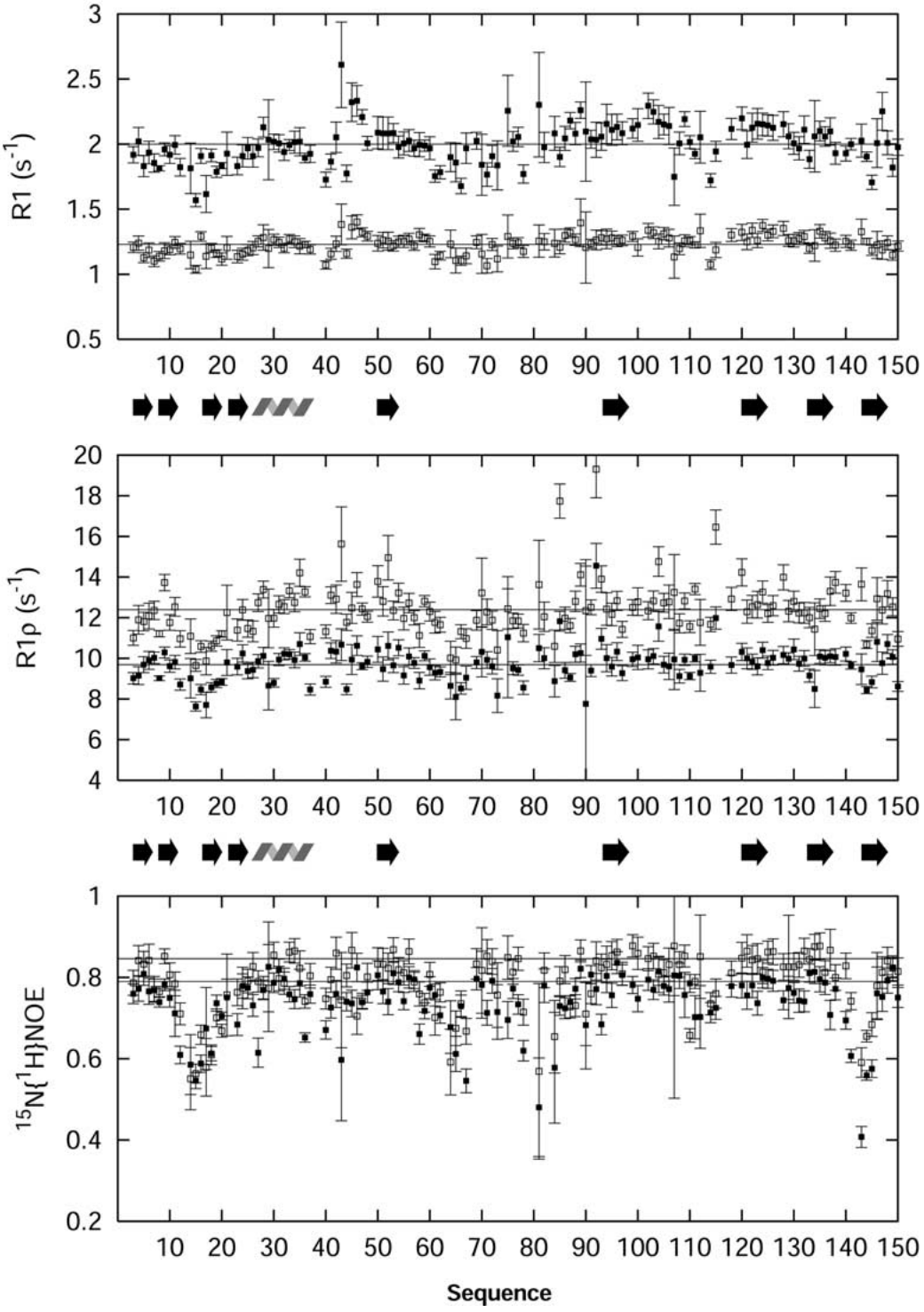

Figure 1. α-Sarcin ^{15}N backbone amide relaxation parameters. Values at 11.7 T and 17.6 T are represented as filled and open squares, respectively. The horizontal lines represent the mean values for each parameter except for the $^{15}N\{^{1}H\}$-NOE graph where the theoretical maximum values are shown (0.79 at 11.7 T and 0.85 at 17.6 T). Secondary structure elements are shown as arrows (β-strands) and a zigzag ribbon (α-helix).

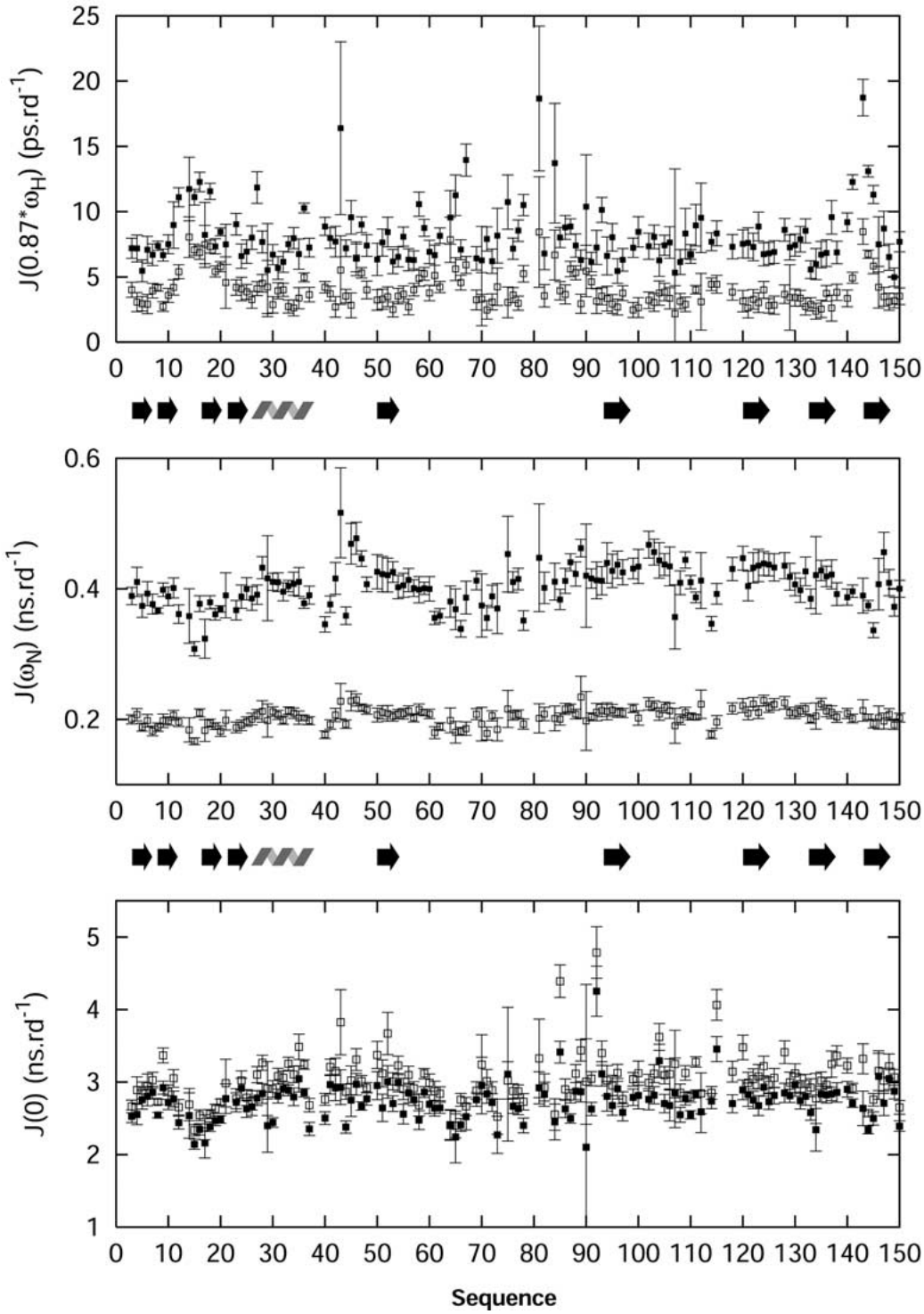

Figure 2. α-Sarcin sequence distribution of the spectral density values mapped at different frequencies. Filled squares represent the data obtained at 11.7 T (0, 50 and 434 MHz) and open squares represent the data at 17.6 T (0, 75 and 653 MHz).

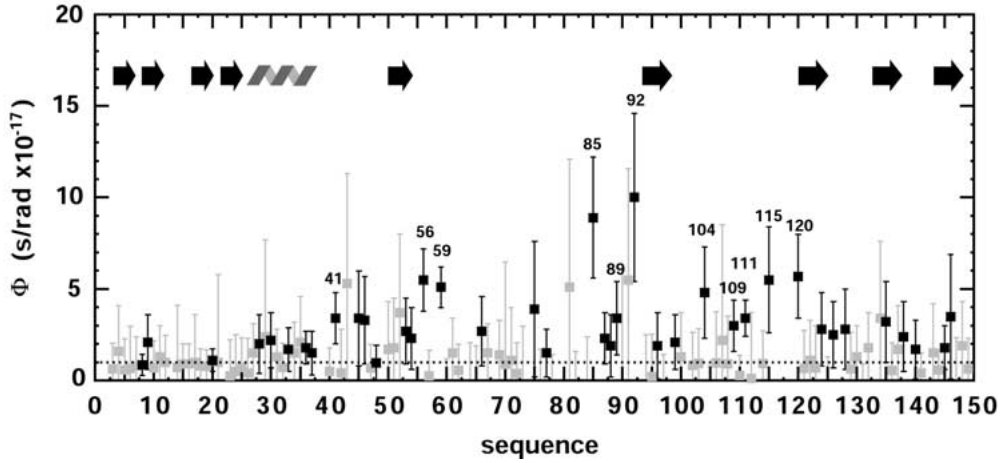

Figure 3. Distribution of the exchange factors obtained from the analysis of the field dependence of J(0) (see Materials and Methods). The residues for which the lower limit of the Φ value (considering its error) is positive have been depicted in black, and the remaining residues in grey.

close to the theoretical maximum at each field (horizontal lines in NOE graph, Figure 1). The $R_{1\rho}(90°)$ distribution shows a profile where secondary elements present high values, indicating that the relaxation of these amide ^{15}N is dominated by the overall tumbling. Other regions (14–20; 64–67; 114–115; and 142–145) have $^{15}N\{^1H\}$-NOE values below the mean and, to a lower extent, low $R_{1\rho}(90°)$ and R_1 values, accounting for dynamic processes occurring in the fast (ns-ps) time scale. Finally, several residues, scattered throughout the sequence, appear to have an extra contribution to the $R_{1\rho}(90°)$, probably arising from the existence of slower processes, in the μs to ms time scale. The sets of relaxation parameters at both fields were analysed from two different approaches: reduced spectral density mapping (Peng and Wagner, 1992a,b; Farrow et al., 1995; Ishima and Nagayama 1995a,b; Lefèvre et al., 1996) and model-free formalism (Lipari and Szabo, 1982; Clore et al., 1990).

Reduced spectral density mapping

Figure 2 shows the sequence distribution of the five spectral density values sampled at 0, 50, 75, 434 and 653 MHz frequencies. Like in the case of transverse relaxation rates, exchange contributions lead to an increase of the J(0) values, which depends on the square power of the B_0 strength. The residues affected by this extra contribution can be identified by a visual inspection of the J(0) graph, since they have large and field dependent values. However, we have screened these exchange contributions more carefully by combining the two sets of J(0) values as previously described (see Materials and Methods). Figure 3 shows the result of this analysis as a sequence distribution of Φ values (Equation 2). It should be noticed that the errors in many cases are larger than the actual value (grey dots) and the corresponding residues have been ignored. Of the remaining residues (black dots) only a few (41, 56, 59, 85, 89, 92, 104, 109, 111, 115 and 120) have high enough Φ values and corresponding low enough errors to indicate with confidence that they are truly involved in μs to ms dynamic processes. All of these residues are outside the regular elements of secondary structure.

Ignoring the spins with exchange contributions, regions 27–37, 50–53, 94–97, 120–124, 133–138, 144–147 show the highest J(0) values and low values for $J(\omega_H)$, which indicate a negligible contribution of fast internal dynamics to the relaxation of these spins. J(0) can be approximately described as $2/(5\tau_m)$, and the mean value along these regions provides a rough estimate of the overall correlation time (6.8 ± 0.7 at 11.7 T and 7.8 ± 0.6 ns at 17.6 T).

A more precise value of the overall tumbling time of the molecule was obtained from the parameters derived from the linear fitting of the $J(\omega_N)$ versus J(0) (Figure 4), once they were substituted in the Lefèvre equation. Two of the three roots of this equation directly provide the correlation time for the overall tumbling (τ_m) and the generalised time for faster internal motions (τ_I). The two values of τ_m, 7.82 ± 0.05 and 7.79 ± 0.05 ns, obtained from the 11.7 and 17.6 T

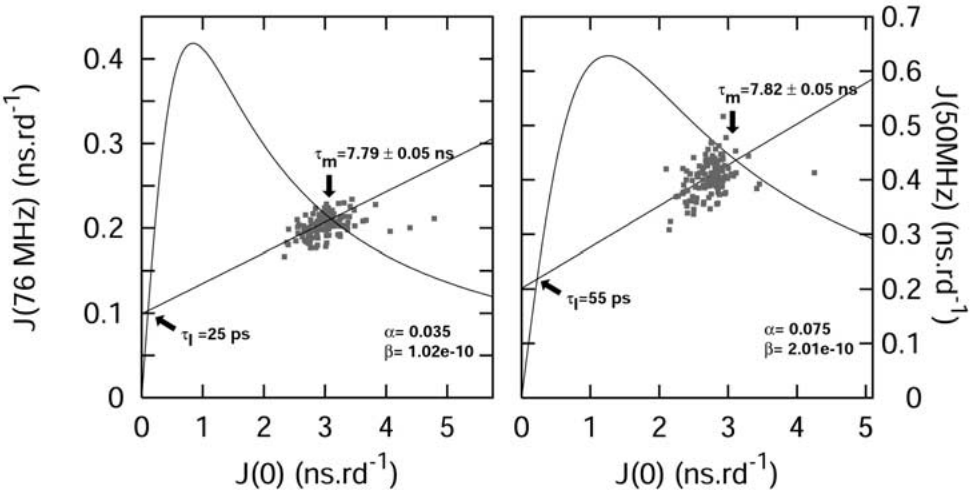

Figure 4. Relationships between $J(\omega_N)$ and J(0) at 11.7 (left) and 17.6 T (right). The curve represents the theoretical variation between both parameters assuming a simple lorentzian form for the spectral density function. Experimental data (grey squares) fits to the linear function with parameters α and β. Both functions crossover at points corresponding to the overall correlation time (τ_m) and a generalized time for the internal motions (τ_I).

data sets, are in excellent agreement with each other, showing the robustness of the method.

Graphs in Figure 4 show most of the experimental points clustered nearby the crossing point demarcating the τ_m boundary, and indicating a limited contribution of internal motions faster than τ_m. Note that the two crossing points in the graphs correspond to the roots on Equation 3. Those data points close to the τ_I boundary correspond to residues with fast internal dynamic contributions, whereas those undergoing slower dynamics are placed at J(0) values above the τ_m boundary.

The $J(\omega_N)$ values provide valuable information that is free of exchange contributions. The J(75) values show a flat distribution indicating that the sampled frequency is nearby the isosbestic point of $J(\omega)$ (where the internal dynamic contributions, faster that the overall tumbling, are negligible) (Guignard et al., 2000). When sampling below this frequency a pattern for J(50) is found similar to that of J(0), with low values for the flexible regions and high values for the rigid ones. The secondary structure elements and parts of the loops are among these last but, interestingly, the highest J(75) values are found for residues of loop 1 (44, 46 and 47) which are involved in non-regular ternary interactions in the structure (Pérez-Cañadillas et al., 2000).

Model-free analysis

The model-free analysis has been carried out with the Modelfree 4.01 program (Mandel et al., 1995; Palmer et al., 1991) kindly provided by Prof Palmer, Columbia University. We have used the first (lower energy) conformer of the ensemble deposited within the PDB (access code 1DE3) throughout the analysis. Statistical analysis of a selected subset of spins (belonging to rigid parts of the protein, according to criteria described elsewhere (Mandel et al., 1995)) reveals that α-sarcin behaves as an axially symmetric rotor with the major diffusion axis nearly collinear to the principal component of the inertial tensor (F-test 10.65 and p-value 1.25×10^{-5} compared to the isotropic model). A similar statistical analysis between axial symmetric and anisotropic models reveal no significant improvement (F-test 0.27 and p-value 0.76). The rotational diffusion parameters were further optimised in the last stage of the calculation, simultaneously with the internal dynamics parameters (after the internal spectral density functions were chosen). The final parameters were $D_{||}/D_{\perp} = 1.16 \pm 0.02$ and τ_m (iso) $= 7.54 \pm 0.02$ ns slightly smaller to those determined from the spectral density mapping. With respect to the internal dynamics, 86 spins are satisfactorily represented by model 1 (S^2), 25 by model 2 (S^2,τ_{int}), 4 by model 3 (S^2,R_{ex}), 5 by model 4 (S^2,τ_{int}, R_{ex}) and 7 by model 5 (S_f^2,S_s^2,τ_{int}). These have been colour coded in the S^2 graph in Figure 5. A comparison between the backbone RMSDs of α-sarcin NMR structures (Pérez-Cañadillas et al., 2000) and the S^2 values obtained here show a reasonably good correlation (not shown). The lowest S^2 values are found for

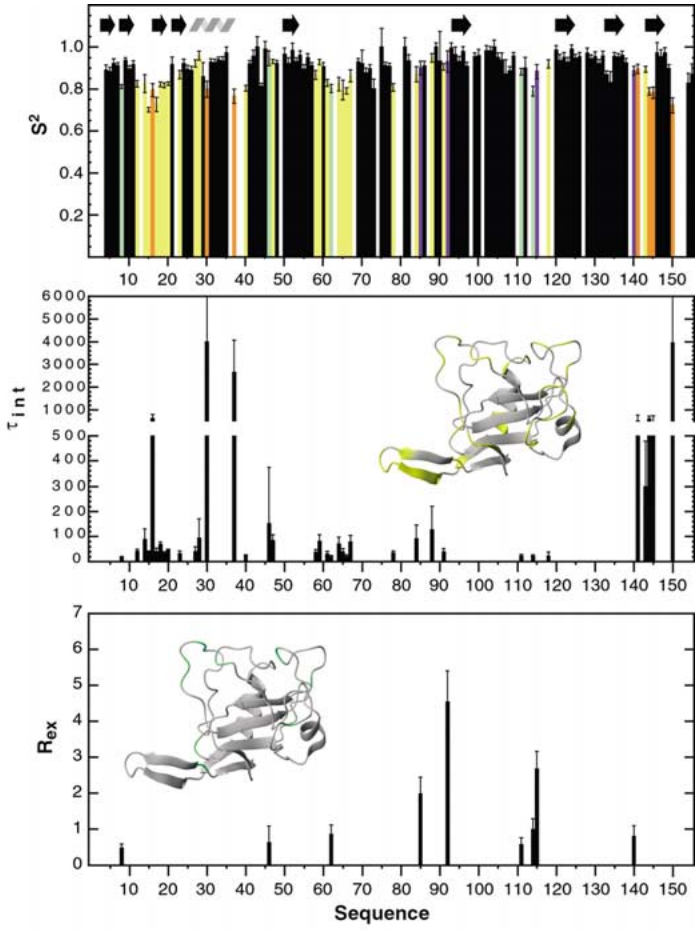

Figure 5. Model-free analysis summary. The upper graph shows the sequence distribution of order parameters (S^2), the bars have been coloured according to the spectral density model used in the analysis: model 1 (S^2) in black, model 2 (S^2, τ_e) in yellow, model 3 (S^2, R_{ex}) in green, model 4 (S^2, τ_e, R_{ex}) in blue and model 5 (S_s^2,S_f^2, τ_e) in orange. The S^2 values for the indol nitrogens of Trp 4 and 51 have been included as residues 154 and 155. The middle graph represents the distribution of residues having fast internal dynamics contributions. The data has been plotted with two different time scales: 0–500 for models 2 and 4 and 500–6000 for model 5. The α-sarcin ribbon model in the graph shows the three-dimensional distribution of these residues (in yellow). The residues having chemical exchange contributions are plotted in the lower graph, together with a ribbon representation showing their 3D distribution (in green). The protein structure representations have been generated with the program MOLMOL (Koradi et al., 1996).

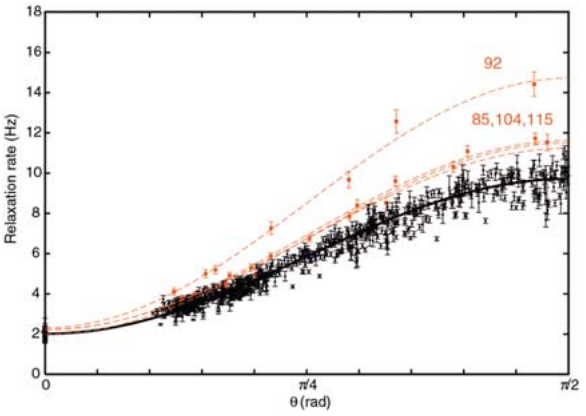

Figure 6. Plot of the experimental off-resonance $R_{1\rho}$ for α-sarcin as a function of the tilt angle θ of the effective spin-lock field with respect to the static magnetic field. The solid black line represents the theoretical behaviour on the basis of R_1 and $R_{1\rho}(90°)$ mean values. Best-fit curves and data for residues with exchange contribution (labelled) have been plotted separately (red dashed lines and squares).

the less well-defined regions in the structure, pointing to a dynamic explanation for the larger RMSD values rather than to a lack of experimental data. It is of note the large number of residues with restricted internal dynamics ($S^2 > 0.9$), which includes the ones in secondary structure elements (except β_{2B} and part of β_7), in part of the first loop (residues 40–48), in the first half of loop 3 (99–109), in loop 4 (125–130) and in several stretches of loop 2 (54–58, 69–71, 75–77, 81–82, 86–94). On the other hand, the most mobile parts of the protein are: the β-turn and the strand β_{2B} of the N-terminal hairpin, the connection between α-helix and loop 1, residues 60–66 in loop 2, second half of loop 3 (111–115) and most of loop 5 and strand β_7 (140–145). Amide vectors having additional relaxation contributions from internal motions (τ_{int} and R_{ex} in Figure 5) are also concentrated in these areas.

The number of residues found to have exchange contributions using model-free analysis (Figure 5) is considerably less than when the isotropic model is used (data not shown). It is well known that simplified isotropic models, in which anisotropy is neglected can wrongly lead to a number of artefactual exchange terms (Tjandra et al., 1995). Four residues (85, 92, 115 and 140) best fit to the model having only an R_{ex} term (model 3) and another five (8, 46, 62, 111 and 114) to the model also including fast internal dynamics (model 4). All of them lay outside regular secondary elements and four show clear R_{ex} contributions (85, 92, 111 and 115) in the spectral density mapping analysis (see above). The largest exchange terms have been found for residues 85, 92 and 115, a feature that also correlates with the spectral density analysis. In contrast, chemical exchange contribution have been found for residues 41, 56, 59, 104 and 120 in the reduced spectral density mapping but not in the model-free analysis.

Off-resonance $R_{1\rho}$ relaxation

Figure 6 shows the dependence of $R_{1\rho}$ as function of the tilt angle (θ). A theoretical curve using the mean relaxation rates at 11.6 T ($\langle R_1 \rangle = 2.0\ s^{-1}$, $\langle R_2 \rangle = 9.7\ s^{-1}$) has been included as a reference. Most of the experimental data points are clustered around this curve, pointing to a similar behaviour for these residues, which essentially constitute the rigid core of the protein. However, there are some outliers. Some of them, have a lower $R_{1\rho}$ and are in regions involved in fast (ns-ps) internal dynamics. Others, with experimental data points above the theoretical curve, are likely to be involved in slow (μs to ms) internal motions. According to this analysis, four residues (104, 115, 85 and specially 92) appear to have conformational exchange contributions in the μs to ms time scale. All these residues have previously been identified by spectral density and/or model-free analysis. Unfortunately, the poor quality of the $R_{1\rho}(90°)$ adjustments (Equation 7, data not shown) makes it impossible to extract reliable τ_{ex} values for these residues.

Hydrodynamics calculations

The results of the hydrodynamic calculations are shown in Table 1 and Figure 7. The optimal AER (atomic element radius) value of 2.9 Å was chosen by comparing the calculated R_2/R_1 ratio with the experimental data (at 11.6 T and 11.7 T) following a recently described protocol (Bernadó et al., 2002). In this case, the predicted thickness of hydration shell for α-sarcin (0.9–1.1 Å) can be obtained from the difference between the AER value and the van der Walls radii (typically 1.8–2.0 Å) (García de la Torre et al., 2000). The calculated correlation time (7.67 ns) and axial anisotropy (1.36) are in good agreement with the ones derived from the analysis of NMR data (7.54 ± 0.02 ns and 1.16 ± 0.02). Finally the calculated R_1 and R_2 values are compared to the experimental data in Figure 7. The calculated values (open squares) reflect only the effect of the rotational anisotropy and, as expected, the agreement between predicted and experimental values is lower in the regions affected by internal flexibility (i.e., N-terminal hairpin, residues 85, 92 and 115). Back-calculated relaxation data by hydrodynamic methods provide an independent way to analyse the relaxation data. Moreover the method could be useful to discern between relaxation contributions arising from diffusion anisotropy, which are likely to be well predicted from the simulation, from those coming from internal motions, surely misrepresented by a rigid model. How to represent these internal motions in the bead-like hydrodynamic model is a question that remains open in our view and it is not clear to what extent these motions would affect the outcome of the calculations.

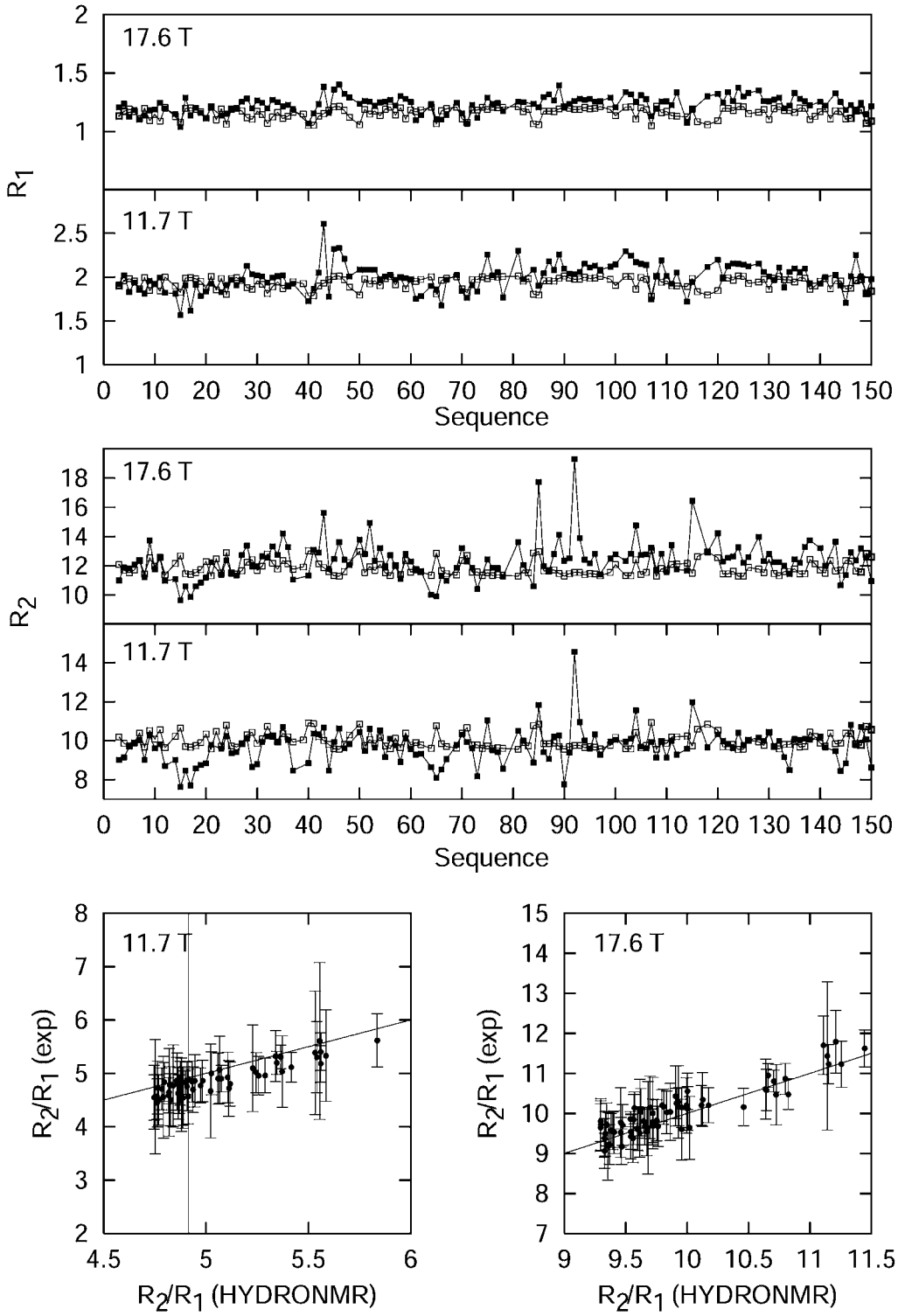

Figure 7. Comparison between experimental (solid) and HYDRONMR calculated (open) R_1 and $R_{1\rho}(90°)$ values and comparison between experimental and calculated R_2/R_1 ratios. Experimental values were filtered with 0.5 times the standard deviation of ∇ (see Bernadó et al., 2002, for details).

Table 1. Hydrodynamic calculation summary for α-sarcin. [a]Calculations have been performed with the program HYDRONMR (García de la Torre et al., 2000), with AER = 2.9 Å, T = 308 K and η = 72 centipoise. [b]Spectral density mapping

	HYDRONMR[a]	Experimental	
		Modelfree	SDM[b]
$D_t \times 10^{-6}$ cm^2 s^{-1}	1.45		
Radius of gyration $\times 10^{-7}$ cm	1.61		
$D_x \times 10^{-7}$ s^{-1}	2.65		
$D_y \times 10^{-7}$ s^{-1}	1.89		
$D_z \times 10^{-7}$ s^{-1}	1.98		
$2D_z/(D_x+D_y)$	1.36	1.16	
$\tau_c \times 10^{-9}$ s	7.67	7.54	7.8

Discussion

Overall tumbling

The experimental value of the overall correlation time (7.54 ns from the model-free approach and 7.82/7.79 from the spectral density mapping analysis) for α-sarcin is in good agreement with the calculated value from the hydrodynamic analysis (7.67 ns). Moreover, both methods also agree about the anisotropy of the rotational diffusion, indicating that the molecule behaves as a prolate (axially symmetric) rotor. The choice of a more elaborated diffusion model than isotropic, avoids the false identification of R_{ex} terms, even in cases like the α-sarcin, which show only small anisotropy. However, selection of a rotational diffusion model should be statistically tested to avoid overinterpretation of the data. In this context we found that hydrodynamic calculations can provide another method to explore the diffusion properties, and back-calculation of NMR relaxation data, which, in conjunction with the classical Model-free and Spectral Density Mapping approaches, can give a wider perspective in protein dynamics studies. In addition, hydrodynamic calculations provide additional information such as hydration, radius of gyration, and the translational diffusion coefficient that can be compared to the experimental value measured by NMR.

To date, rotational dynamics has been studied by NMR for more than one hundred proteins and a general correlation between size and rotational tumbling can be derived. However, the results presented here show that α-sarcin (16.9 KDa) tumbles faster (7.8 ns) than other proteins of similar size with the exception of cyclophilin (Krishnan and Cosman, 1998). A correlation between a fast global correlation time and a lack of internal mobility has been shown for flavodoxin (Zhang et al., 1997). Although the case of α-sarcin is not as dramatic, we observe highly restricted internal dynamics for most of the backbone HNs (∼75% having S^2 values over 0.9). Another explanation for this slightly enhanced overall tumbling could lie in the hydration properties. As mentioned before, the hydrodynamic calculation predicts a very thin hydration shell (0.9–1.1 Å). Similar hydration shells have been predicted for savinase, cytochrome b5 and Calbindin-D9k (García de la Torre et al., 2000). Experimental calorimetric (Cantor and Schimmel, 1980) and X-ray diffraction studies (Jiang and Brunger, 1994) suggest a mono-layer of solvent for globular proteins and usually only 20% to 70% of this mono-layer is needed to reproduce experimental data in hydrodynamic calculations (Korzhnev et al., 2001, and references therein). The thickness of the hydration shell has no significant effect on the rotational anisotropy predictions but it has a dramatic effect on the absolute rates of translation and diffusion. The predicted NMR values are also strongly sensitive to it and in fact they can be used to adjust hydrodynamic parameters as we have shown here. This idea has been explored in a recent hydrodynamic study on a selected group of globular proteins (Bernadó et al., 2002). Thus, ^{15}N relaxation data is useful to choose the atomic radius element AER in the hydrodynamic calculations, and an empirical range between 2.8 and 3.8 Å, centered at 3.3 Å has been found (Bernadó et al., 2002). The AER value obtained for α-sarcin (2.9 Å) is within this range but deviated towards the lower limit. Low AER values may be related to large-scale motions. In α-sarcin,

the N-terminal hairpin protrudes outwards in the 3D structure and shows a significant mobility on the fast time scale (see below). This region, aligned with the major axis of the axial tensor, is very important for the anisotropic behaviour of the molecule and even moderate-amplitude motions in this part might modulate the protein's rotational diffusion properties. Thus, internal mobility in the N-terminal hairpin would decrease the degree of rotational anisotropy (notice that the calculated value from the hydrodynamic calculations is slightly higher than the one obtained from the relaxation analysis) and perhaps also decrease the optimum AER value.

ps to ns dynamics

Fast internal dynamics occur mainly in the closed end of the N-terminal hairpin, in loop 5, in the first turn of the α-helix and in a stretch of residues at the beginning of loop 2 (58–67). Structural mapping of these residues (Figure 5 middle) shows that nearly all are located near the surface. Residues of the protein core have very restricted internal dynamics.

In a previous study (Pérez-Cañadillas et al., 2000) we compared the flexibility of the N-terminal hairpin in α-sarcin with that in the highly homologous restrictocin (85% sequence identity with α-sarcin). In the crystal structure of the latter, that segment was completely disordered as revealed by the absence of electron density in that region (Yang and Moffat, 1996). This higher flexibility in restrictocin was interpreted as due to the lack of an equivalent salt bridge to that between Lys 11 and Glu 140 in α-sarcin. Our results show that this region is also flexible in α-sarcin, but probably not as much as the corresponding region of restrictocin. This fact may be of importance for the distinctive stability and catalytic properties of the two proteins. Site directed mutagenesis (García-Ortega et al., 2001) indicates that the N-terminal hairpin may play some role in α-sarcin's membrane interaction, cytotoxicity and ribonuclease activity. Those properties were tested in α-sarcin, restrictocin and the single K11L α-sarcin mutant. Restrictocin and the K11L mutant (both lacking the Lys 11 and Glu 140 salt bridge) were found to be less effective than α-sarcin in both inhibiting cellular protein biosynthesis and perturbing the phospholipid bilayer (García-Ortega et al., 2001).

μs to ms dynamics

According to our data, few residues in α-sarcin are involved in μs to ms internal dynamics. Only residues 85, 92 and 115 have been consistently identified using different analysis formalisms as being affected by conformational exchange contributions. Glutamic acid 115 is placed in the middle of loop 3 and its backbone carbonyl forms a hydrogen bond to the ring phenol group of Tyr 106. The resonances of the aromatic protons of Tyr 106 are broad at 293 K (data not shown), indicating that the presence of motions of this aromatic side chain is in the sub-second to millisecond time scale. Due to the large chemical shift anisotropy of the aromatic rings, their reorientation could provide an effective relaxation mechanism for their neighbouring residues (Guignard et al., 2000), as it is seen to occur in the case of residue 115. Exchange contributions of lower magnitude have been found in the model-free analysis in residues close to 115 (46, 111 and 114).

An interpretation of the remaining residues presenting exchange contributions is not straightforward. His 92 amide ^{15}N has the highest R_{ex} term (see Figures 4 and 5) and although it is buried inside the protein (∼0% accessibility for the HN over the 20 member ensemble in 1DE3) it does not form any intramolecular hydrogen bond. The presence of an unfulfilled hydrogen bond in a low dielectric medium like the interior of a protein is energetically very unfavourable. However, a closer analysis of the structure revealed the presence of a 16 $Å^3$ cavity between loops 2 and 4 and the back face of the central β-sheet (Pérez-Cañadillas et al., 2000), which is large enough to accommodate at least one water molecule. The amide proton of His 92 points toward the cavity and could potentially interact with a structural water molecule inside it. Therefore the exchange contribution observed for His 92 might be related to the presence of the hypothetical structural water. Apart from the NMR structure, there is no additional experimental data that supports the existence of this cavity, thus hydration studies could provide future insights on it. We have analysed the X-ray structure of the α-sarcin homologue restrictocin (Yang and Moffat, 1996, PDB code 1AQZ) and found a cavity in the vicinity of His 91 (structurally equivalent to His 92 in α-sarcin). One of the water molecules in this structure (H_2O 757) close to this cavity, forms a hydrogen bond with the side chain of His 91.

Asp 85 is placed in loop 2 and a R_{ex} term has been consistently found for its backbone ^{15}N in all analyses. However, it is difficult to assign this contribution to any particular dynamic process. As in the case of His 92, Asp 85 HN is buried within the structure and it does not form any intramolecular hydrogen bond; both

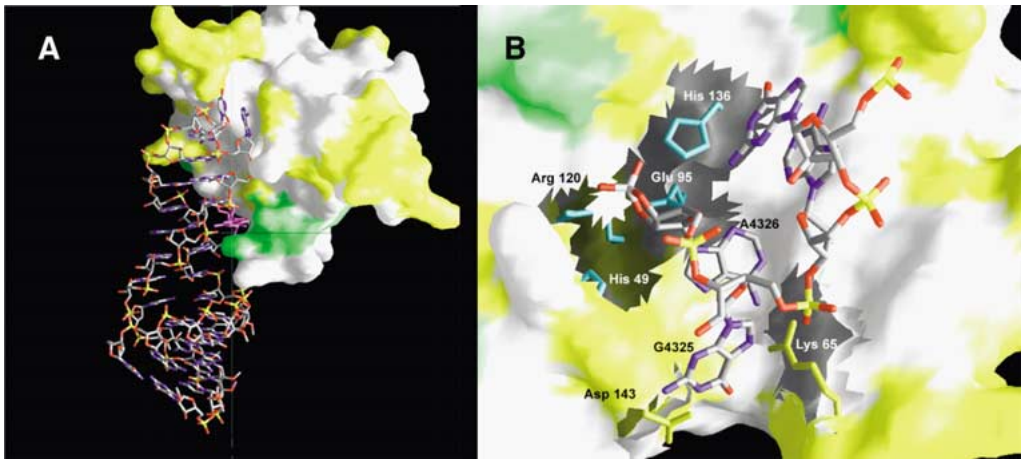

Figure 8. Protein surfaces involved in substrate recognition present different dynamic properties. X-ray structure of restrictocin-inhibitor complex in the (A) 'bound' and in (B) 'misdocked' forms (Yang et al., 2001, PDB codes 1JBS, 1JBR). The protein is represented by its molecular surface whereas the RNA is represented by a stick model. (A) Residues recognising the budged guanine (in magenta) are shadowed in green. They correspond to residues in free α-sarcin that have dynamic contributions in the ms to μs time scale. (B) Recognition site of the 'flipped out' purine bases G4325 and A4326 in the tetra loop RNA sequence. Residues shadowed in yellow correspond to flexible regions in free α-sarcin with motions in the ns to ps time scale, and residues in white correspond to rigid regions in free α-sarcin. The active site residues in blue have been also represented as a reference.

features are seen in the equivalent residue (Asn 84) in restrictocin. Another shared feature between both structures is that the following residue is a glycine (86 in α-sarcin and 85 in restrictocin) has a positive ϕ angle, so the detected high R_{ex} could be explained by some local conformational changes such as, i.e., a concerted 180° flip of the 85–86 peptide bond.

Finally, residues Glu 140 and Asn 8 also adjust to models with exchange contribution in the Lipari-Szabo approach. Residue 8 is placed in the hinge region at the middle of the N-terminal hairpin whereas residue 140 is in loop 5. Both residues are in close contact in the 3D structure so their slow scale contributions may have the same dynamic origin. A hinge motion of the closed end of the N-terminal hairpin and/or a conformational change in residue 140 (which has an unusual ϕ positive angle) are likely to be the sources of such motions.

Biological implications

The structural bases of the specific cytotoxic activity of α-sarcin have been previously proposed based on a model of its complex with RNA (Yang and Moffat, 1996, Pérez-Cañadillas et al., 2000). The model showed that the key bulged guanine G4319, the only nucleotide known to be critical for recognition in the SRL (sarcin/ricin loop), could be recognised by one or more side chains between Ser 110 and Lys 114, and is in complete agreement with mutagenesis data (Kao and Davies, 1999). Recently, crystal structures of α-sarcin's homologue, restrictocin, complexed with inhibitor RNA molecules, have been published (Yang et al., 2001). Interestingly, the structural data from these complexes support most of the protein interactions previously derived from the docking model. Thus, upon complex formation, only minor rearrangements are provoked in the protein moiety, whereas the GAGA tetraloop suffers a dramatic change from its free structure. The unfolding of the RNA tetraloop appears to be a requirement for its recognition and cleavage (Yang et al., 2001). However it is not clear whether the protein induces this energetically penalised conformational change, or if it binds and stabilises a minor RNA conformation.

At the interface between restrictocin and RNA, the region around the bulged guanine (G4319) shows specific side chain interactions with lysine residues 110, 111 and 113. We have carefully compared the restrictocin structures of the free enzymes (restrictocin 1AQZ and α-sarcin 1DE3) with the 'bound' form of restrictocin (1JBS). A first visual inspection does not reveal any major changes on the overall folding of the loop directly involved in the bulged guanine recognition. However a more careful analysis shows a backbone conformational change in restrictocin upon binding. Lys 110 ψ angle suffers a nearly 180° rotation, driving the residue to the beta region of the

Ramachandran plot and the ϕ angle of the next residue (Lys 111) is also rotated to a positive value in a less populated region of the Ramachandran plot. Remarkably, the corresponding region in α-sarcin (110–114) is involved in chemical exchange processes on the μs to ms time scale, a common feature of residues belonging to macromolecular interfaces. Even more, Lys 111 (equivalent to Lys 110 in restrictocin) shows this contributions itself. These results suggest that these relaxation properties can be related with this conformational change. It is at least striking that this unique dynamic 'hot-spot' (Figure 8A) is the one involved in the above mentioned intermolecular interactions.

Although the X-ray structure (Yang et al., 2001) is miss-docked by one nucleotide, some insights into the tetraloop recognition site can be derived. In the GAGA region, A4326 (the flipped out base prior the scissile bond) makes contacts with the backbone amides of residues 52 to 54. Our dynamic results with α-sarcin show that this stretch of residues is essentially frozen in the molecular framework. This rigidity found in the base recognition site (50–54) could be a requisite for the selective sequence recognition. NMR studies on RNase T1 (Fushman et al., 1994) show that the base pocket (41–44) is one of the most dynamic region of the protein (contributions on the μs-ms time scale). In contrast, our data suggests that only bases from a specific sequence that can be exactly accommodated in the rigid pocked of α-sarcin can be properly recognised. Guanine 4325 is also flipped out contacting Asp 143 and Lys 65 sidechains (Figure 8B). The structurally equivalent residues of α-sarcin show faster dynamic contribution than the overall molecular tumbling.

Additionally, it has been recently proposed (García-Ortega et al., 2002) that the N-terminal hairpin (residues 1–26) of α-sarcin can recognize other regions of the ribosome distant from SRL. Interestingly, in spite of being a regular secondary structural element, this part of the protein is one of the most mobile as it has low S^2 values and a high proportion of residues with internal dynamics (Figure 5).

In summary, α-sarcin shows different degrees of internal mobility among key residues involved in substrate recognition: from the backbone rigidity of residues implicated in the base recognition site, to the flexibility (in different time scales) exhibited by residues involved in binding the bulged guanine, the scissile-turn, and the new proposed place of interaction. The exact role played by motions of different time scales and amplitudes in the conformational change of the SRL will require additional experiments. However, it is clear that for α-sarcin recognition, a delicate dynamic balance among the recognition elements seems to be as crucial as the three-dimensional arrangements. Thus, in the α-sarcin/SRL complex the presence of a certain degree of flexibility among the interacting surfaces should be desired, whereas a highly mobile interface could compromise the specificity of the interaction.

Acknowledgements

We thank Dr H. Videler and Dr D.V. Laurents for their helpful suggestions during the preparation of this manuscript. This work was supported by the Dirección General de Investigación Científica y Técnica (Spain) (PB98-0677) and by the Dirección General de Enseñanza Superior (Spain) (BMC2000-0551). JMPC would like to gratefully acknowledge the EMBO and the European Union for support through their long-term post-doctoral fellowship.

References

Abragam, A. (1961) *Principles of Nuclear Magnetism*, Clarendon Press, Oxford, U.K.

Akke, M. and Palmer III, A.G. (1996) *J. Am. Chem. Soc.*, **118**, 911–912.

Atwell, S., Ultsch, M., De Vos, A.M. and Wells, J.A. (1997) *Science*, **278**, 1125–1128.

Banci, L., Bertini, I., Cavazza, C., Felli, I.C. and Koulougliotis, D. (1998) *Biochemistry*, **37**, 12320–12330.

Bernadó, P., García de la Torre, J. and Pons, M. (2002) *J. Biomol. NMR*, **23**, 139–150.

Cantor, C.R. and Schimmel, P.R. (1980) *Biophysical Chemistry. Part II: Techniques for the Study of biological Structure and Function*, Freeman, San Francisco, CA.

Carrasco, B. and García de la Torre, J. (1999) *Biophys. J.*, **76**, 3044–3057.

Clackson, T. and Wells, J.A. (1995) *Science*, **267**, 383–386.

Clore, G.M., Szabo, A., Bax, A., Kay, L.E. Driscoll, P.C. and Gronenborn, A. (1990) *J. Am. Chem. Soc.*, **112**, 4989–4991.

Delaglio, F., Grzesiek, S., Vuister, G.W., Zhu, G., Pfeifer J., and Bax, A. (1995) *J. Biomol. NMR*, **6**, 277–293.

Farrow, N.A., Muhandiram, R., Singer, A.U., Pascal, S.M., Kay, C.M., Gish, G., Shoelson, S.E., Pawson, T., Forman-Kay, J.D. and Kay, L.E. (1994) *Biochemistry*, **33**, 5984–6003.

Farrow, N.A., Zhang, O., Szabo, A., Torchia, D.A. and Kay, L.E. (1995) *J. Biomol. NMR*, **6**, 153–162.

Feher, V.A. and Cavanagh, J. (1999) *Nature*, **400**, 289–293.

Fushman, D., Weisemann, R., Thüring, H. and Rüterjans, H. (1994) *J. Biomol. NMR*, **4**, 61–78.

García de la Torre, J., Huertas, M.L. and Carrasco, B. (2000) *J. Magn. Reson.*, **B147**, 138–146.

García-Ortega, L., Lacadena, J., Mancheño, J.M., Oñaderra, M., Kao, R., Davies, J., Olmo, N., Martínez del Pozo, A. and Gavilanes, J.G. (2001) *Protein Sci.*, **10**, 1658–1668.

García-Ortega, L., Masip, M., Mancheño, J.M., Oñaderra, M., Lizarbe, M.A., García-Mayoral, F., Bruix, M., Martínez del Pozo, A. and Gavilanes, J.G. (2002) *J. Biol. Chem.*, in press.

Guignard. L., Padilla, A., Mispelter, J., Yang, Y.S., Stern, M.H., Lhoste, J.M. and Roumestand, C. (2000) *J. Biomol. NMR*, **17**, 215–230.

Ishima, R. and Nagayama, K. (1995a) *Biochemistry*, **34**, 3162–3171.

Ishima, R. and Nagayama, K. (1995b) *J. Magn. Reson.*, **B108**, 73–76.

Jiang, J.S. and Brünger, A.T. (1994) *J. Mol. Biol.*, **243**, 100–115.

Kao, R. and Davies, J. (1999) *J. Biol. Chem.*, **274**, 12576–12582.

Koradi, R., Billeter, M. and Wüthrich, K. (1996) *J. Mol. Graph.*, **14**, 51–55.

Korzhnev, D.M., Billeter, M., Arseniev, A.S. and Orekhov, V.Y. (2001) *Prog. Nucl. Magn. Reson. Spectrosc.*, **38**, 197–266.

Kraulis, P.J. (1989) *J. Magn. Reson.*, **24**, 627–633.

Kraulis, P.J., Domaille, P.J., Campbell-Burk, S.L., van Aken, T. and Laue, E.D. (1994) *Biochemistry*, **33**, 3515–3531.

Krishnan, V.V. and Cosman, S. (1998) *J. Biomol. NMR*, **12**, 177–182.

Lacadena, J., Martínez del Pozo, A., Barbero, J.L., Mancheño, J.M., Gasset, M., Oñaderra M., López-Otín, C., Ortega, S., García, J.L. and Gavilanes J.G. (1994) *Gene*, **142**, 147–151.

Lacadena, J., Martínez del Pozo, A., Martínez-Ruiz, A., Pérez-Cañadillas, J.M., Bruix M., Mancheño, J.M., Oñaderra, M. and Gavilanes, J.G. (1999) *Proteins: Struct. Funct. Genet.*, **37**, 474–484.

Lee, L.K., Rance, M., Chazin, W.J. and Palmer 3rd A.G. (1997) *J. Biomol. NMR*, **3**, 287–298.

Lefèvre, J.-F., Dayie, K.T., Peng, J.W. and Wagner, G. (1996) *Biochemistry*, **35**, 2674–2686.

Lipari, G. and Szabo, A. (1982) *J. Am. Chem. Soc.*, **104**, 4546–4570.

Mandel, A.M., Akke, M., Palmer III, A.G. (1995) *J. Mol. Biol.*, **246**, 144–163.

Mittermaier, A., Varani, L., Muhandiram, D.R., Kay, L.E. and Varani, G. (1999) *J. Mol. Biol.*, **294**, 967–979.

Mulder, F.A., de Graaf, R.A., Kaptein, R. and Boelens. R. (1998) *J. Magn. Reson.*, **131**, 351–357.

Mulder, F.A., van Tilborg, P.J., Kaptein, R. and Boelens, R. (1999) *J. Biomol. NMR*, **13**, 275–288.

Olmo, B.H., Turnay, J., de Buitrago, G.G., López de Silanes, I., Gavilanes, J.G. and Lizarbe, M.A. (2001) *Eur. J. Biochem.*, **268**, 2113–2123.

Olson, B.H. and Goerner, G.L. (1965) *Appl. Microbiol.*, **13**, 314–321.

Palmer III, A.G., Rance, M. and Wright, P.E. (1991) *J. Am. Chem. Soc.*, **113**, 4371–4380.

Peng, J.W. and Wagner, G. (1992a) *J. Magn. Reson.*, **98**, 308–332.

Peng, J.W. and Wagner, G. (1992b) *Biochemistry*, **31**, 8571–8586.

Peng, J.W. and Wagner, G. (1995) *Biochemistry*, **34**, 16733–16752.

Pérez-Cañadillas, J.M., Campos-Olivas, R., Lacadena, J., Martínez del Pozo, A., Gavilanes, J.G., Santoro, J., Rico, M. and Bruix, M. (1998) *Biochemistry*, **37**, 15865–15876.

Pérez-Cañadillas, J.M., Santoro, J., Campos-Olivas, R., Lacadena, J., Martínez del Pozo, A., Gavilanes, J.G., Rico, M, and Bruix, M. (2000) *J. Mol. Biol.*, **299**, 1061–1073.

Szyperski, T., Luginbuhl, P., Otting, G., Guntert, P. and Wuthrich, K. (1993) *J. Biomol. NMR*, **3**, 151–164.

Tjandra, N., Feller, S.E., Pastor, R.W. and Bax, A. (1995) *J. Am. Chem. Soc.* **117**, 12562–12566.

Turnay, J., Olmo, N., Jiménez, A., Lizarbe, M.A. and Gavilanes, J.G. (1993) *Mol. Cell. Biochem.*, **122**, 39–47.

Wang, C., Pawley, N.H. and Nicholson, L.K. (2001) *J. Mol. Biol.*, **313**, 873–887.

Woessner, D.T. (1962) *J. Chem. Phys.*, **37**, 647–654.

Wool, I.G. (1984) *Trends Biochem. Sci.*, **9**, 14–17.

Wool, I.G. (1997) Structure and mechanism of action of cytotoxic ribonuclease α-sarcin. In *Ribonucleases: Structure and Function*, D'Alessio, G. and Riordan, J.F. (Eds.), Academic Press, San Diego, pp. 131–159.

Yang, X. and Moffat, K. (1996) *Structure*, **4**, 837–852.

Yang, X, Gérczei, T., Glover, L. and Correll, C.C. (2001) *Nat. Struct. Biol.*, **11**, 968–973.

Zhang, P., Dayie, K.T. and Wagner, G. (1997) *J. Mol. Biol.*, **272**, 443–455.

Zinn-Justin, S., Berthault, P., Guenneugues, M. and Desvaux, H. (1997) *J. Biomol. NMR*, **10**, 363–372.